Combined magnetic and gravity measurements probe the deep zonal flows of the gas giants

E. Galanti ⬤★ and Y. Kaspi

Department of Earth and Planetary Sciences, Weizmann Institute of Science, Rehovot, Israel 7610001

ABSTRACT

During the past few years, both the *Cassini* mission at Saturn and the *Juno* mission at Jupiter provided measurements with unprecedented accuracy of the gravity and magnetic fields of the two gas giants. Using the gravity measurements, it was found that the strong zonal flows observed at the cloud level of the gas giants are likely to extend thousands of kilometres deep into the planetary interior. However, the gravity measurements alone, which are by definition an integrative measure of mass, cannot constrain with high certainty the exact vertical structure of the flow. Taking into account the recent *Cassini* magnetic field measurements of Saturn, and past secular variations of Jupiter's magnetic field, we obtain an additional physical constraint on the vertical decay profile of the observed zonal flows on these planets. Our combined gravity–magnetic analysis reveals that the cloud-level winds on Saturn (Jupiter) extend with very little decay, i.e. barotropically, down to a depth of around 7000 km (2000 km) and then decay rapidly in the semiconducting region, so that within the next 1000 km (600 km) their value reduces to about 1 per cent of that at the cloud level. These results indicate that there is no significant mechanism acting to decay the flow in the outer neutral region, and that the interaction with the magnetic field in the semiconducting region might play a central role in the decay of the flows.

Key words: planets and satellites: atmospheres – planets and satellites: detection – planets and satellites: gaseous planets – planets and satellites: general – planets and satellites: interiors – planets and satellites: magnetic fields.

1 INTRODUCTION

The strong east–west zonal winds at the cloud level of Jupiter and Saturn have been observed to be largely stable over the past several decades, based on the detection of cloud motion (Sánchez-Lavega, Rojas & Sada 2000; Porco et al. 2003; García-Melendo et al. 2011; Tollefson et al. 2017). The winds on Jupiter are organized in alternating zonal jets that reach ∼140 m s^{-1} at low latitudes, with a strong asymmetry between the jets around latitude 20° north and south. The winds on Saturn are mostly hemispherically symmetric, with a wide, strong eastward flow of nearly 300 m s^{-1} at the equatorial region, and alternating mid-latitude jets that are weaker and less hemispherically symmetric (Fig. 1, black). On both planets, the observations carry uncertainties from different sources, of up to ±50 m s^{-1} on Saturn (García-Melendo et al. 2011) and up to ±20 m s^{-1} on Jupiter (Tollefson et al. 2017; Fletcher et al. 2020). In addition, since the winds are measured relative to some reference rotation rate, uncertainty in Saturn's spin implies a possible range of the wind velocities, depending on whether the *Voyager*-based rotation (Smith et al. 1982) or the more recently calculated faster rotation rates (Helled, Galanti & Kaspi 2015; Mankovich et al. 2019) are used (Fig. 1, white shading). In spite of the multitude of observations of the cloud-level winds, the only direct measurement below the cloud level comes from the *Galileo* probe at Jupiter, which showed that at latitude 6.5°N the zonal wind increases

with depth in the top few bars and then remains nearly constant (barotropic) down to 21 bars (130 km deep; Atkinson, Pollack & Seiff 1996).

Recently, the latitudinally dependent gravity fields of Jupiter and Saturn were measured with high accuracy by the *Juno* and *Cassini* spacecraft, respectively. On Jupiter, the gravity field was found to have significant hemispherical asymmetries (Iess et al. 2018), which can be explained by the cloud-level winds extending deep into the planet (Kaspi 2013; Kaspi et al. 2018). On Saturn, even the symmetric part of the gravity field was found to differ substantially from that predicted with a rotating rigid body, especially for the higher gravity harmonics (Iess et al. 2019; Fig. 1, blue). This difference was attributed to the winds extending thousands of kilometres deep (Galanti et al. 2019). For both planets, the gravity measurements indicate not only the overall depth of the winds but also that the same meridional profile of the zonal flows likely extends to these depths (Kaspi et al. 2020).

The measurements of the gravity field, which is by definition an integrative measure of mass, cannot constrain with high certainty the detailed vertical structure of the flow, since different distributions of density anomalies can be expressed in the same gravity field at the planet's surface (Galanti & Kaspi 2017c). Therefore, in both planets, the solutions for the flow fields discussed above are not unique (see discussion in Kaspi et al. 2018 & 2020), and other solutions that are not tied to the cloud-level winds can be found to give an exact match to the gravity measurements, as discussed for Jupiter (Kong et al. 2018) and Saturn (Qin et al. 2020). However, given the small

★ E-mail: eli.galanti@weizmann.ac.il
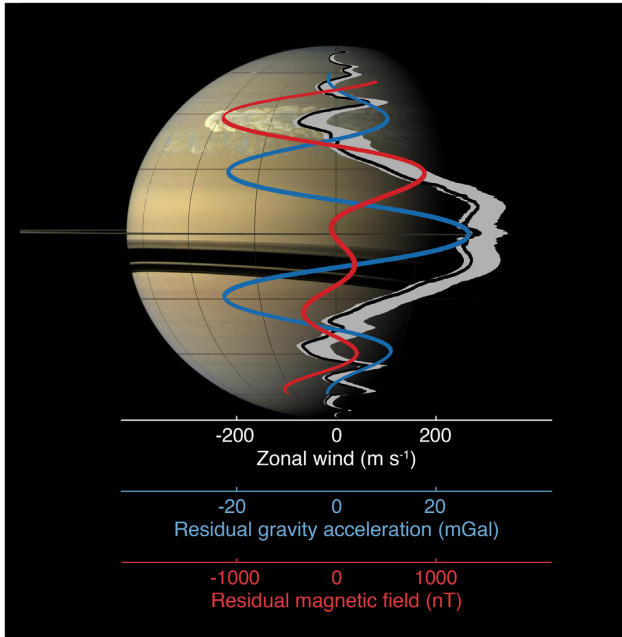
Figure 1. The three measurements used in this study to calculate the Saturnian flow structure; the cloud-level wind (García-Melendo et al. [2011]) adjusted with the recently estimated rotation period of 10 h 34 min (Helled et al. [2015]; Mankovich et al. [2019]; black) and a range of winds calculated for rotation periods between 10 h 32 min (Read, Dowling & Schubert [2009]) and 10 h 39 min (Smith et al. [1982]; white shading); the residual gravity field at the planet's surface R_S (blue) based on the dynamical contribution to gravity harmonics J_3 and J_5 to J_{10} (Galanti et al. [2019]; Iess et al. [2019]); and the residual radial magnetic field at $0.875R_S$ (red) based on the measured Gauss coefficients g_4^0 to g_{11}^0 (Dougherty et al. [2018]; Cao et al. [2020]). All values composing the gravity and magnetic fields appear in Table 1. Measurements are shown on top of a Saturn picture taken during the *Cassini* mission (NASA/JPL-Caltech).

number of gravity measurements in both planets, and the fact that taking the observed cloud-level flows and extending them into the interior in a simple way match both in sign and in magnitude the measured gravity harmonics give a good indication that indeed the interior flows resemble those at the cloud level. Furthermore, the flow structures suggested in Kong et al. (2018) and Qin et al. (2020) exhibit a flow of the order of $1\,\mathrm{m\,s}^{-1}$ at depths of $0.2R$ for Jupiter and $0.3R$ for Saturn. However, while not fully determined, current estimates of the conductivity at these depths (Liu, Goldreich & Stevenson [2008]; Wicht et al. [2019b]) would imply a generation of a very strong Lorentz force, which would act to diminish the flow (Cao & Stevenson [2017b]; Duer, Galanti & Kaspi [2019]; Moore et al. [2019]). Finally, in a recent study, a wide range of possible flow structures was examined in the context of the Jupiter gravity measurements (Duer, Galanti & Kaspi [2020]). Varying both the cloud-level wind profiles and the way the wind decays with depth, it was found that while the measured gravity field can be explained by various flow structures, within the range examined in the study, solutions that differ considerably from the observed cloud-level winds are statistically unlikely.

Both missions have also measured at an unprecedented accuracy the magnetic fields of both planets, which differ dramatically between the two planets. On Jupiter, the field has a complex latitudinal and longitudinal structure (Connerney et al. [2018]), a characteristic that might be exploited to constrain the flow structure using magnetic secular variations (SVs; Duer et al. [2019]; Moore et al. [2019]). Conversely, the magnetic field on Saturn is extremely axisymmetric

(Dougherty et al. [2018]; Cao et al. [2020]), with latitudinal variability reflecting not only low-order harmonics but also the contribution from higher harmonics (Fig. 1, red), which may be related to the structure of the flow below the cloud level (Gastine et al. [2014]; Cao & Stevenson [2017b]).

On both planets, the magnetic field measurements provide valuable information that can potentially be used to further constrain the structure of the zonal winds below the cloud level. Here, we report, for the first time, on the well-confined structure of the flow field of Saturn, calculated based on the measured cloud-level wind and both the gravity and magnetic measurements. We then extend our analysis to include the structure of Jupiter's flow field, using both the measured gravity field and the estimated SVs of the measured magnetic field.

2 METHODS

2.1 The thermal wind balance

Large-scale flows on rapidly rotating planets have a direct relation to density anomalies and, therefore, affect the gravity field if the flows are deep enough (i.e. involve a large mass; Hubbard [1999]; Kaspi et al. [2010]). Such a flow is governed by a geostrophic balance between the anomalous pressure gradient and the Coriolis force (Pedlosky [1987]; Kaspi, Flierl & Showman [2009]). Given that on Saturn and Jupiter the flow is predominantly zonally symmetric and assuming sphericity (Galanti, Kaspi & Tziperman [2017b]), the resulting vorticity dynamical balance is between the flow gradient in the direction parallel to the axis of rotation and the meridional gradient of density perturbations, known as thermal wind (TW) balance, given by

$$2\Omega r \frac{\partial}{\partial z}(\rho_0 u) = g_0 \frac{\partial \rho'}{\partial \theta}, \tag{1}$$

where $u(r, \theta)$ is the zonal flow field, Ω is the planet's rotation rate, $\rho_0(r)$ and $g_0(r)$ are the rigid-body density and gravity fields, respectively, $\rho'(r, \theta)$ is the anomalous density field, and z is the direction of the axis of rotation. Note that this is not the standard atmospheric form of the TW equation (Holton [1992]) as the derivative on the left-hand side is not in the radial direction, but in the direction of the spin axis (Kaspi et al. [2009]). Other effects not included in this balance, such as the anomalous gravity and centrifugal forces induced by the density anomalies (Zhang, Kong & Schubert [2015]; Cao & Stevenson [2017a]), were shown, for the large-scale zonal flows, to have a small effect on the gravity solutions (Galanti et al. [2017b]; Kaspi et al. [2018]), and therefore are not taken into account here. For the background density $\rho_0(r)$, we use the same profiles as were used in the gravity-only studies for Saturn (Galanti et al. [2019]) and Jupiter (Kaspi et al. [2018]).

The anomalous density field ρ' can then be used to calculate the wind-induced gravity harmonics

$$\Delta J_n^{\mathrm{mod}} = -\frac{2\pi}{MR^n} \int_{-\pi/2}^{\pi/2} \cos\theta\,\mathrm{d}\theta \int_0^R r^{n+2}\mathrm{d}r\, P_n(\sin\theta)\rho'(r, \theta)\mathrm{d}r, \tag{2}$$

where $\Delta J_n^{\mathrm{mod}}$, $n = 2, \ldots, N$ are the coefficients of the wind-induced gravity harmonics, R is the planetary radius, and M is the planetary mass. This principle was successfully used to calculate the overall depth of the winds on Jupiter and Saturn using the *Juno*- and *Cassini*-measured gravity field (Kaspi et al. [2018]; Galanti et al. [2019]; Iess et al. [2019]). For the case of Jupiter, the calculation was based on the odd gravity harmonics only (Kaspi et al. [2018]), and for the case of

Saturn also the even harmonics were used, with the expected rigid-body solution subtracted from the measurements (Fig. 1, blue; see also Table 1a). These are the solutions we reinvestigate in this study with the new constraints from the magnetic field measurements.

2.2 The mean-field electrodynamic balance

The large-scale flow field in Saturn and Jupiter can be also related to a residual magnetic field, induced by the flow in the semiconducting region where the fluid begins to become conductive (Cao & Stevenson 2017b; Galanti, Cao & Kaspi 2017a; Duer et al. 2019). The steady-state balance between the residual magnetic field and the flow, named the mean-field electrodynamics (MFED) balance (Cao & Stevenson 2017b), is

$$\eta_E \left(\nabla^2 - \frac{1}{s^2} \right) B + \frac{1}{r} \frac{d\eta_E}{dr} \frac{\partial(rB)}{\partial r} = -\boldsymbol{B}_0 \cdot \nabla u, \tag{3}$$

$$\eta_E \left(\nabla^2 - \frac{1}{s^2} \right) A = -\alpha B, \tag{4}$$

where $A(r, \theta, t)$ and $B(r, \theta, t)$ compose the residual magnetic field $\boldsymbol{B} = \nabla \times (A\hat{e}_\phi) + B\hat{e}_\phi$, $\boldsymbol{B}_0 = B_0^r \hat{e}_r + B_0^\theta \hat{e}_\theta$ is the background planetary magnetic field, $\eta_E(r)$ is the effective magnetic diffusivity that is inversely proportional to the electrical conductivity σ, and $s = r\sin\theta$ is the distance from the axis of rotation. The function $\alpha(r, \theta) = \alpha_0 \frac{\eta_0}{\eta} \mathrm{erf}(\frac{\theta}{0.005\pi})$ is the dynamo α-effect (Cao & Stevenson 2017b), where $\alpha_0 = 10^{-4}$ m s^{-1} is the value at the base of the semiconducting region (set by taking the convective velocity there as 1 mm s^{-1}, and assuming that the effective dynamo alpha-effect is 10 per cent of the velocity) and η_0 is the value of the magnetic diffusivity at the base of the semiconducting region.

In this study, we set the electrical conductivity σ as an analytical function (Cao & Stevenson 2017b) that reproduces well the measured values (Liu et al. 2008; French et al. 2012). The outer boundary is set where $\sigma = 10^{-4}$ S m^{-1} ($0.9R_S$ for Saturn and $0.98R_J$ for Jupiter), and the inner boundary is set where $\sigma = 10^3$ S m^{-1} ($0.845R_S$ for Saturn and $0.93R_J$ for Jupiter) following Cao & Stevenson (2017b). The transition depth is set where $\sigma = 0.01$ S m^{-1}, resulting in $R_T = 0.875R_S$ for Saturn and $R_T = 0.972R_J$ for Jupiter. Note that the transition depth R_T might be defined differently (Wicht et al. 2019b); however, this should not affect substantially our results, as long as the conductivity profile remains the same. The model solution is given in terms of the Gauss coefficients g_n^0, similar to the measurements (Table 2). The relation between the Gauss coefficients and the latitude-dependent magnetic field in the radial direction (Dougherty et al. 2018), estimated at the transition depth R_T, is given by

$$B_r(\theta) = \sum_n (n+1) \left(\frac{R}{R_T} \right)^{n+2} g_n^0 P_n(\sin\theta). \tag{5}$$

In the MFED balance, it is assumed that the background field is known, and the residual field induced by the flow is small in comparison to the background. Saturn's measured magnetic field (Dougherty et al. 2018), given in terms of the Gauss coefficients g_i^0 (Table 2), can be separated into the main field, composed of g_1^0 through g_3^0 (used as the background field), and the residual (potentially wind-induced) field, composed of g_4^0 through g_{11}^0 (Fig. 1, red), potentially related to the flow field. The separation into the main and residual fields stems from the significant reduction in the value of g_4^0 compared to g_3^0 (a factor of $\sim$25), and might be attributed to the existence of both a deep dynamo and an outer shallow dynamo (Dougherty et al. 2018). A recent analysis of the Saturn magnetic

field (Cao et al. 2020) has pointed to a very similar behaviour, with similar conclusions regarding the possibility that the residual field is induced by the flow in the semiconducting region. None the less, it can be argued that in the newer analysis (Cao et al. 2020; in which g_{12}^0 to g_{14}^0 are also calculated), aside from g_3^0, g_4^0, and g_6^0, the higher Gauss coefficients roughly correspond to a straight line in the Lowes–Mauersberger power spectrum (Lowes 1974), which is an indication that higher harmonics are being generated by the internal dynamo. As we will demonstrate, even if part of the residual magnetic field is not induced by the flow, the results presented here regarding the flow structure in the semiconducting region remain the same. We therefore separate the measured gravity field into the main field composed of g_1^0 to g_3^0, and the residual (potentially wind-induced) field composed of g_4^0 to g_{11}^0, which we attribute to the flow field. For simplicity, we set the background magnetic field $\boldsymbol{B}_0$ as a function of g_1^0 only (Equation 5). Including g_2^0 and g_3^0 causes the wind-induced residual magnetic field to have a somewhat smaller amplitude, but does not change qualitatively any of the results reported here.

The constraint on the flow structure used to calculate the decay function in the semiconducting region is taken as the magnitude of the magnetic field B_r, calculated as the root mean square (RMS) defined between 60°S and 60°N

$$I = \sqrt{ \frac{3}{2\pi} \int_{-\pi/3}^{\pi/3} B_r(\theta)^2 \, d\theta }, \tag{6}$$

being for the measured field $I = 560$ nT for Saturn. Using the MFED model, we calculate I for different combinations of the two parameters defining the decay function Q in the semiconducting region: $0 < f_M < 1$ and 50 km $< H_M < 800$ km (see Section 2.3).

In the MFED approximation, all the non-axisymmetric dynamics are parametrized for (using the dynamo α-effect), and only the axisymmetric magnetic field is solved for. This is an excellent assumption for Saturn (García-Melendo et al. 2011; Dougherty et al. 2018), while for Jupiter where the magnetic field was found to exhibit strong east–west variations (Connerney et al. 2018) a method based on magnetic SVs is more appropriate (Duer et al. 2019; Moore et al. 2019). Another requirement for using the MFED balance is that the magnetic Reynolds number would satisfy $R_m(u) < 1$ (Cao & Stevenson 2017b). In Appendix D, we demonstrate that this is indeed the case for Saturn and Jupiter. Few other factors might affect the MFED solutions: First, the rotation period of Saturn is still not fully known. In this study, we use the more recent estimates of 10 h 34 min, but other rotation periods cannot be excluded. While it was shown that the rotation period has very little effect on the wind-induced gravity harmonics (Galanti & Kaspi 2017), it might have an effect on the latitudinal variability of the residual magnetic field. Secondly, the electrical conductivity used in this study is based on a limited set of measurements and is estimated to have two orders of magnitude uncertainty (Liu et al. 2008). In Appendix C, we discuss in detail how this uncertainty affects our solutions. Finally, a more complex α-effect with latitudinal dependence, as well as the γ-effect (Kapyla et al. 2006), is certainly possible and might be calculated from 3D dynamo models, but there is currently uncertainty of what values should be used for Saturn. However, while adding complexity to the solutions, including these parameters should not change the main results reported here.

Table 1. (a) The Saturn gravity harmonics J_2 to J_{10}. Shown are the *Cassini* measurements (Iess et al. 2019), the rigid-body contribution based on an average of ensemble model solutions (Galanti et al. 2019), the dynamical contribution calculated as the difference between the measurements and the rigid-body contribution, the gravity-optimized solution (Galanti et al. 2019) based on the gravity measurements only, the new gravity-optimized and MFED-restricted solution, where the MFED restricts the inner part of the decay profile but is not optimized for, and the new gravity and MFED-optimized solution where the cloud-level wind is optimized to allow a fit for both gravity and magnetic fields. Note that J_2 and J_4 are not optimized for. (b) The Jupiter gravity harmonics. Shown are the dynamical contributions (measured odds and estimated evens; Kaspi et al. 2020), the solution based only on the gravity measurements (Kaspi et al. 2018), and the new gravity-optimized and MFED-restricted solution. Note that in the Jupiter case, only J_3, J_5, J_7, and J_9 are optimized for.

Gravity harmonics $\times 10^8$	(a) Saturn						(b) Jupiter		
	Cassini measurement	Rigid-body contrib.	Dynamical contrib. (ΔJ_n)	Gravity optimized	Gravity optimized + MFED restricted	Gravity optimized + MFED optimized	*Juno* dynamical contrib. (ΔJ_n)	Gravity optimized	Gravity optimized + MFED restricted
J_2	$1629\,057.33 \pm 2.8$	$1630\,000$	-142.67	5053.98	-1053.70	-117.35	0	54.62	39.57
J_3	5.89 ± 2.3	0	5.89	8.73	7.60	7.13	-4.24	-5.71	-3.96
J_4	$-93\,531.36 \pm 3.7$	$-92\,576.65$	-955.71	758.83	156.90	229.23	0	-5.18	-3.05
J_5	-22.41 ± 5.4	0	-22.41	-25.24	-21.94	-20.63	-6.90	-7.73	-7.10
J_6	8633.99 ± 8.7	8232.55	401.44	409.32	404.04	406.24	1.00	0.33	-0.34
J_7	10.77 ± 12.2	0	10.77	11.04	6.20	8.42	12.39	12.77	12.94
J_8	-1462.36 ± 20.5	-922.60	-539.77	-550.55	-543.50	-532.08	3.50	5.41	4.01
J_9	36.91 ± 26.1	0	36.91	38.06	37.48	39.11	-10.58	-8.84	-7.83
J_{10}	467.24 ± 42.1	118.79	348.45	366.00	352.85	362.47	-3.00	-5.36	-3.12
RMSE	$-$	$-$	$-$	0.61	0.34	0.38	$-$	0.94	0.41

Table 2. The Gauss coefficients composing the magnetic field of Saturn. Shown are the *Cassini* measurements (Dougherty et al. 2018), the gravity-optimized and MFED-restricted solution, and the optimized model solution corresponding to column 7 in Table 1. Note that in column 3 none of the Gauss coefficients are optimized for, and in column 4, g_1^0, g_2^0, and g_3^0 are not optimized for.

Magnetic Gauss coefficients	*Cassini* measurements	Gravity optimized + MFED restricted	Gravity optimized + MFED optimized
g_1^0	$21\,140.2 \pm 1.0$	1452.1	543.9
g_2^0	1581.1 ± 1.2	-67.0	-2.1
g_3^0	2260.1 ± 3.2	693.0	217.4
g_4^0	91.1 ± 4.2	14.2	95.6
g_5^0	12.6 ± 7.1	-54.3	8.8
g_6^0	17.2 ± 8.2	29.4	18.1
g_7^0	-59.6 ± 8.1	-35.4	-47.5
g_8^0	-10.5 ± 8.7	4.6	-5.7
g_9^0	-12.9 ± 6.3	11.1	-12.7
g_{10}^0	15.0 ± 7.0	-11.1	3.8
g_{11}^0	18.2 ± 7.1	-0.3	26.3
RMSE	$-$	7.69	0.99

2.3 Definition of the flow structure

In all variants of flow structure discussed in this study, the same flow field is used to generate both the gravity and the magnetic fields. We start by taking the observed meridional profile of wind at the cloud level (Fig. 1, black line, for Saturn, and Fig. 4b, grey line, for Jupiter) and decompose it into the first N Legendre polynomials

$$u^{\mathrm{obs}}(\theta) = \sum_{i=0}^{N} A_i^{\mathrm{obs}} P_i(\sin\theta), \qquad (7)$$

where A_i^{obs} are the coefficients determining the latitudinal shape of the observed wind, θ is the latitude, P_i are the Legendre polynomials, and $N = 99$ is the number of polynomials to be used. Defining a

modified cloud-level wind

$$u^{\mathrm{sol}}(\theta) = \sum_{i=0}^{N} A_i^{\mathrm{sol}} P_i(\sin\theta), \qquad (8)$$

where A_i^{sol} are the modified coefficients, we allow these coefficients to vary during the optimization process while making sure they do not deviate considerably from their observed values. Note that we construct the wind using a very large number of polynomials to allow the wind solution to follow closely the observed wind. The optimization procedure described in Appendix A ensures that the large number of coefficients is well constrained. Next, the modified cloud-level wind $u^{\mathrm{sol}}(\theta)$ is projected parallel to the axis of rotation (Kaspi et al. 2009) to get the basic non-decaying field $u_0(r, \theta)$. This field is then decayed in the radial direction to give

$$u(r, \theta) = u_0(r, \theta)Q(r), \qquad (9)$$

where r is the radial direction. The decay function $Q(r)$ is defined as

$$Q(r) = \tanh\left(\frac{r - R_{\mathrm{T}}}{\delta H_{\mathrm{T}}}\right) \frac{1 - f_{\mathrm{M}}}{\tanh\left(\frac{R - R_{\mathrm{T}}}{\delta H_{\mathrm{T}}}\right)} + f_{\mathrm{M}}, \quad R_{\mathrm{T}} < r < R, \qquad (10)$$

$$Q(r) = f_{\mathrm{M}} \exp\left(\frac{r - R_{\mathrm{T}}}{H_{\mathrm{M}}}\right), \quad r \leq R_{\mathrm{T}}, \qquad (11)$$

where δH_{T} is the width of the hyperbolic tangent function, f_{M} is the ratio between the flow strength at the transition depth and the flow at the cloud level, and H_{M} is the decay scale height in the inner layer. This functional form of the flow's radial decay allows two distinctly different behaviours in the regions above and below the transition depth R_{T}. In the outer region, the decay function represents a non-magnetic dynamical effect, with the baroclinic shear being in TW balance (Kaspi et al. 2009), and the free parameter δH_{M} allowing a range of decaying profiles, from a gradual decay to a case where the cloud-level winds keep their value almost constant until reaching the transition depth. In the inner region, the exponential decay function is assumed to be a result of the increased electrical conductivity σ. Based on the choice of the parameters A_i^{sol}, f_{M}, H_{M}, and δH_{T},

the flow structure is defined, and can be used to generate both the wind-induced gravity field and the wind-induced magnetic field.

3 RESULTS

The methodology presented above can be more readily applied to Saturn given its highly axisymmetric magnetic field (Dougherty et al. 2018; Cao et al. 2020), while the magnetic field of Jupiter is highly non-axisymmetric (Connerney et al. 2018; Moore et al. 2018), making the usage of the MFED approximation much more challenging. We therefore first investigate the Saturn case with the combined magnetic–gravity analysis, and then discuss the Jupiter case where we substitute the MFED method with insights gained from past measurements of the planet's magnetic field SVs (Moore et al. 2019).

3.1 The Saturn case

We start by using the Saturn magnetic field to constrain the flow field. This constraint is set by the magnitude of the measured residual magnetic field, defined here as the RMS of the radial component, B_r, between 60°S and 60°N (Fig. 1), calculated to be $I = 560$ nT (equation 6). This is the maximal residual magnetic signature expected from the flow field. By using the MFED balance (Section 2.2) and varying the two parameters defining the flow structure in the semiconducting region, f_M and H_M (Section 2.3), the full range of possible solutions for the wind-induced magnetic field is revealed (Fig. 2a). As expected, higher values of H_M and f_M (deeper flows) give larger magnetic signatures, with H_M being the dominant parameter. Since the measured value of 560 nT can be obtained with different combinations of the two parameters (Fig. 2a, dashed black contour), the zonal wind's radial decay in the semiconducting region cannot be determined uniquely. However, different parameter combinations located along the 560 nT contour give very similar solutions for B_r. For example, the three combinations denoted by the red dots in Fig. 2(a) result in almost identical profiles of B_r (Fig. 2b, red lines). Most importantly, the shape of the new decay profiles in the semiconducting region (Fig. 3a, red lines deeper than the transition depth) is very different from the solution constrained with only the gravity field (Galanti et al. 2019; dashed black line). The magnetic field measurements imply that the flow must decay sharply at the transition depth. This depth is much shallower than the depth where the gradually decaying gravity-only solution loses most of the wind strength. In addition, due to the magnetic field constraint, in the new solution the long tail does not extend deep into the planet's interior (grey area).

3.1.1 A magnetically restricted solution

Having determined the wind decay functions in the semiconducting region that are consistent with the magnetic field measurements (Table 2), an optimal solution is sought for the wind decay function above the transition depth, such that the associated residual gravity field matches the measured gravity field (Appendix A). Using TW balance (Section 2.1), the optimal decay function above the transition depth (Fig. 3a, red lines) and the optimal cloud-level wind structure (Fig. 3b, red lines) are found, such that the resulting wind-induced gravity field best explains the measured residual gravity field (Fig. 1, blue; see also values in Table 1a). Note that since the decay function is optimized only above the transition depth, the solutions still satisfy the magnetic field constraint (Appendix A).
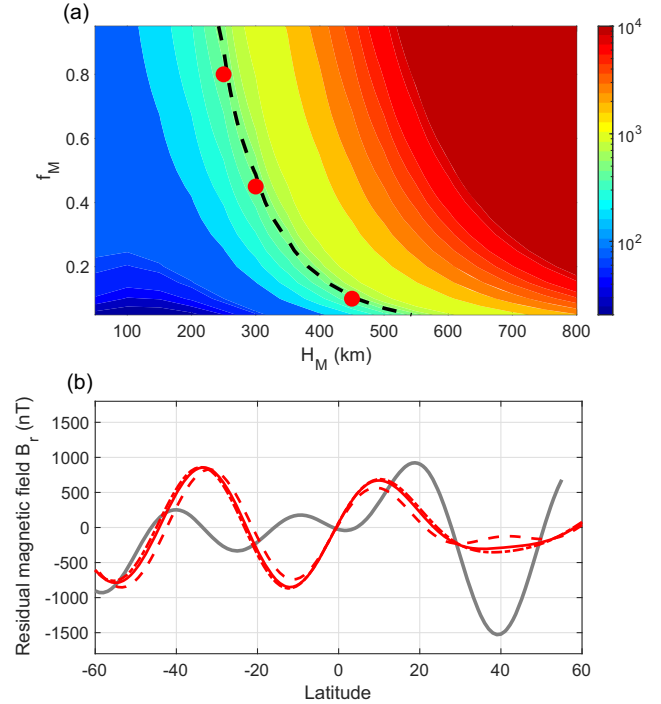
Figure 2. The residual magnetic field induced by the flow structure. (a) The RMS of the residual magnetic field B_r at $0.875R_s$ for a range of flow decay parameters H_M (km) and f_M. Also shown is the value of the measured field of 560 nT (dashed contour) and three representative combinations of parameters matching the measurements: $H_M = 450$, 300, and 250 km and $f_M = 0.1$, 0.45, and 0.8, respectively. (b) The resulting latitude-dependent residual magnetic field B_r for the three representative combinations: dashed, solid, and dashed–doted, respectively. Also shown is the measured field (grey).

All three optimal solutions are within the measurement uncertainty, with an RMS error (equation A4) of 0.34, 0.34, and 0.33 for the main decay profile (solid red) and the two variants (dashed and dotted–dashed), respectively (Table 1a; note that an RMSE of 1 means that the solution harmonics are on average at the measurement error distance from the measurement itself). Note also that the new solutions derived by the magnetic field measurements that dramatically restrict the flow to shallower depth are not deteriorated compared to the gravity-only solution (with an RMSE of 0.61). In fact, they are better solutions in terms of the RMSE (Table 1a). This improvement is predominantly due to the different decay functions used in the semiconducting region. While in the set-up of the gravity-only solution the possible decay function is a combination of synthetic smoother functions, here the physically driven, much sharper decay in the transition depth allows a better fit to the measurements. Moreover, the required modification in the cloud-level wind (Fig. 3b, solid red) is marginal with respect to the gravity-only solution, strengthening the robustness of the wind solution with respect to the observed wind. The shape of the new decay function in the outer neutral region implies that, unlike in the gravity-only solution (Fig. 3a, dashed black), the winds in the new solution barely decay in the first 7000 km below the cloud level (i.e. barotropic); only below that depth a decay commences. Only such strong flow in the outer region can generate sufficient mass advection that would be able to explain the gravity measurements.
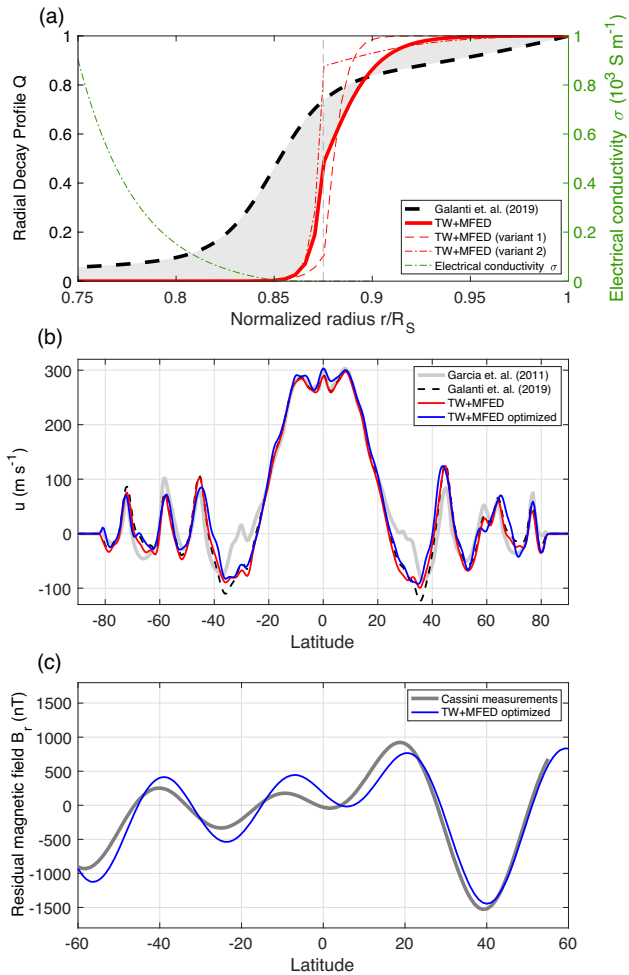
Figure 3. The implication of the magnetic field constraint for Saturn's flow structure. (a) The new solution for the wind's radial decay (solid red) together with the gravity-only constrained solution (Galanti et al. 2019; dashed black). The difference between the solutions is emphasized by the grey area. Also shown are two representative variants of the new solution corresponding to the red dots in Fig. 2(a) (dashed and dotted–dashed red), the conductivity profile σ (S m^{-1}, green), and the transition depth ($0.875 R_S$) separating the outer neutral region and the inner semiconducting region (vertical dashed line). (b) The cloud-level wind profiles. Shown are the observations (García-Melendo et al. 2011; grey), the new solution with the magnetic field restricting the decay profile (red), the fully optimized new solution with the residual magnetic field optimized in addition to the gravity harmonics (blue), and the gravity-only restricted solution (Galanti et al. 2019; dashed black). (c) The magnetic field of the fully optimized solution (blue) and the measured residual magnetic field (Dougherty et al. 2018; grey).

3.1.2 A fully combined gravity–magnetic solution

The new, depth-confined, solution fits all the relevant gravity harmonics (Table 1a) and the magnitude of the residual magnetic field (Fig. 2b, solid red line, and Table 2), but its latitudinal dependence is different from the measured magnetic field. By setting the wind decay profile to the solution already obtained (Fig. 3a, solid red line), we perform a full optimization of the cloud-level wind, looking for a solution for which the values of both the induced gravity and magnetic fields are within the uncertainties of the measurements (Appendix B). We obtain an optimal solution (Fig. 3b, blue line) with an RMSE of 0.38 for the residual gravity field and an RMSE of 0.99 for the residual magnetic field (Fig. 3c and Table 2). Therefore,

with the same decay profile, and with only minor modifications to the cloud-level wind, well within the measurement uncertainty (García-Melendo et al. 2011), a flow field is found that can explain the latitudinal dependence of both the gravity and the magnetic fields. In summary, we find that the values of the higher Gauss coefficients pose an upper bound on the wind-induced magnetic field of Saturn. No matter whether the residual field comes from the winds or the deep dynamo, the contributions of the wind in the semiconducting region to the residual field cannot be higher than the measurements, and this strongly constrains the magnitude of the flow in the semiconducting region.

3.1.3 Applicability of the solution

The ability of the MFED balance to constrain the flow field in the semiconducting region should be examined from several aspects. First, a basic requirement for using the MFED balance is that the magnetic Reynolds number, defined as $R_m(u) = uH_\sigma \sigma \mu_0$ ($H_\sigma = \sigma / \frac{d\sigma}{dr}$ is the scale height associated with it), would satisfy $R_m(u) < 1$ (Cao & Stevenson 2017b). We find that $R_m(u)$ calculated with the optimal flow solution (Fig. 3a) satisfies this condition everywhere (Appendix D). Moreover, the wind-induced residual magnetic field B_r can be roughly related to the background field $\boldsymbol{B_0}$ via $B_r \sim R_m(\alpha)^{\max} R_m(u)^{\max} |\boldsymbol{B_0}|$, where $R_m(\alpha) = \alpha H_\sigma \sigma \mu_0$ is the magnetic Reynolds number associated with the dynamo α-effect (Cao & Stevenson 2017b). Since $R_m(\alpha)$ reaches a maximal value of 0.25 (at the lower boundary of the semiconducting region) and $R_m(u) < 1$ everywhere, the resulting residual magnetic field is always much smaller than the background field (Fig. 2b). Secondly, the MFED balance depends on several parameters that are not strongly constrained. Most importantly, the electrical conductivity σ is known only within two orders of magnitude (Liu et al. 2008). In order to evaluate the effect of this uncertainty on our solution, we examine two extreme cases, for which σ is an order of magnitude larger and lower than the mean value used here (Appendix C). In both cases, solutions for the flow field that satisfy both the magnetic and gravity measurements can be found. In the former case, the solution shows an even more pronounced barotropic behaviour in the outer layers and an even sharper decay of the winds near the transition depth. In the latter case, the solution exhibits a more gradual wind decay, asymptotically getting closer to (but still far from) the gravity-only solution (Fig. B1). Moreover, these results also pose a limit on the uncertainty in the conductivity profile, where conductivity that is two orders of magnitude larger would not allow a physical solution, and that such a limit does not exist for a lower value. Thirdly, the dynamo α-effect, parametrizing the action of the small-scale 3D turbulence on the wind-induced toroidal magnetic field, is assumed in our study to be only a function of depth, with a sign change at the equator (Cao & Stevenson 2017b). In the framework of the MFED balance, the uncertainty associated with the magnitude of α is equivalent to an uncertainty in σ. Therefore, its effect on our solutions is similar to the one discussed in the analysis above. Finally, inhomogeneity of α in space or time might also have an effect on the solution, yet these effects are difficult to estimate, and might be compensated by small alterations to the cloud-level wind.

3.2 The Jupiter case

The above results have direct implications for Jupiter, whose gravity measurements were also used to decipher the flow structure (Iess et al. 2018; Kaspi et al. 2018), and whose optimal radial decay based

on gravity alone was found to be quite gradual. If the mechanisms governing the flow structure are similar to Saturn's, constraining Jupiter's flow with the *Juno* magnetic field measurements should show a sharp shear at a depth of around 2000 km below the cloud level. As the magnetic field of Jupiter is highly non-axisymmetric (Connerney et al. 2018; Moore et al. 2018), using the MFED approximation is much more challenging, since it involves a non-axisymmetric wind-induced magnetic field, making it more difficult to disentangle this field from the internal field. Recently, using a dynamo model, the effect of different flow structures on the magnetic field in the semiconducting region of Jupiter was estimated, yielding the conclusion that the effect might be measurable by the *Juno* mission (Wicht et al. 2019b). However, the Lowes spectrum of the higher magnetic harmonics of Jupiter (Connerney et al. 2018) fits roughly a straight line, suggesting that the internal field might play a dominant role in setting their values (Tsang & Jones 2020). Again, this renders the task of separating the wind-induced magnetic field highly challenging.

The effect of the wind on Jupiter's magnetic field might be identified in the magnetic field's SVs (Ridley & Holme 2016; Duer et al. 2019; Moore et al. 2019). Given that a time span of several years of magnetic field measurements is required for calculating the SVs, an analysis based on the *Juno* measurements is expected to be available only towards the end of the nominal mission (Bolton et al. 2017). However, we can already use the available studies, and the results of this study, to examine the potential implications for Jupiter. It has been shown, based on the past measurements of Jupiter's magnetic field and their decadal SV, that the magnetic drift at a depth of $0.95R_J$ is of the order of a few centimetres per second (Moore et al. 2019). The authors conclude that the flow itself can be restricted to the values of the drift rate at $0.93R_J$, and that Ohmic dissipation considerations limit the flow to an order of 1 m s^{-1} in the $0.94-0.95R_J$ region (Cao & Stevenson 2017b). Since the gravity field is not very sensitive to this region, definitely not to variations of the flow strength below 1 m s^{-1}, we can confidently choose a decay function that generates such a flow.

Assuming that the mechanism governing the structure of the flow is similar to the one we find in Saturn, a flow structure in the semiconducting region (0.95–0.972) can be set such that the above constraint is met (Fig. 4a). The magnetic Reynolds number associated with this solution ensures that the wind-induced residual magnetic field is much smaller than the internal field (Appendix D). Similar to the case of Saturn, we search for a solution for the flow structure in the outer layers ($r > 0.972R_J$) such that the measured odd gravity field is explained. By only slightly varying the cloud-level winds (Fig. 4b), within the measurement uncertainty (Tollefson et al. 2017), we find a solution for the full decay function (Fig. 4a, solid red line). The fit to the gravity field has an RMSE of 0.43, an even better fit to the measurement than the 0.90 achieved with the gravity field alone (Kaspi et al. 2018; see Table 1b). Importantly, the difference (grey area) between the gravity-only solution and the new solution is substantial, even more than the one found in the Saturn case. The new possible solution for Jupiter is of a structure that is remarkably similar to the new solution for Saturn (Fig. 3a, solid red), i.e. almost no decay of the winds from the surface to a depth of around 1800 km, and then a sharp decay over a depth of about 600 km. Similar to the Saturn case, if future studies find the conductivity to be an order of magnitude larger than the values used here (Liu et al. 2008), it will strengthen the conclusion regarding the shape of the wind decay. However, an even larger conductivity does not permit a physical solution. Conversely, if the conductivity is found to be much weaker, then the magnetically constrained solution
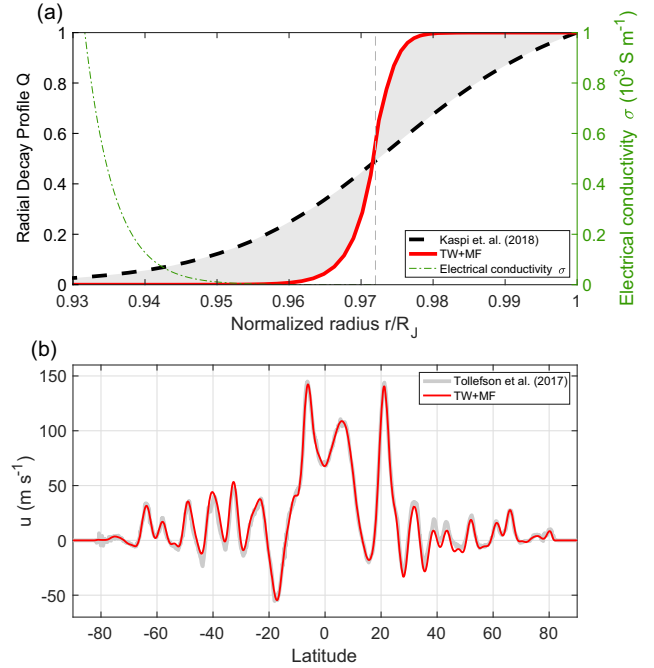
Figure 4. The implication of the magnetic field constraint for Jupiter's flow structure. (a) The new solution for the wind's radial decay (solid red) together with the gravity-only constrained solution (Kaspi et al. 2018) (dashed black). The difference between the solutions is emphasized by the grey area. The decay function in the semiconducting region is defined with $H_M = 200 \text{ km}$ and $f_M = 0.55$, so that the wind is set to about 2 cm s^{-1} at $0.93R_J$ and 0.7 m s^{-1} at $0.95R_J$. In the outer region, the decay function is defined with $\delta H_T = 204 \text{ km}$. Also shown is the conductivity profile σ (green), and the transition depth ($0.972R_J$) separating the outer neutral region and the inner semiconducting region (vertical dashed line). (b) The cloud-level wind profiles. Shown are the observations (Tollefson et al. 2017; grey) and the new solution with the magnetic field restricting the decay profile (red).

will be more gradual, and closer to the one calculated based only on the gravity field.

4 DISCUSSION AND CONCLUSION

The inclusion of the *Cassini* magnetic measurements as an additional constraint on Saturn's flow structure below the cloud level unveils a well-confined flow field that can explain not only the residual magnetic field but also better explain the measured gravity field. Based on constraints from the magnetic SV, a similar structure is plausible also in Jupiter. The sharp baroclinic shear of the flow in the semiconducting region, as well as the barotropic structure of the flow from the cloud level down to the transition depth, suggests that the flow interaction with the magnetic field in the semiconducting region (Liu et al. 2008; Cao & Stevenson 2017b) plays an important role in the wind's decay in the interior of Saturn, Jupiter, and potentially other giant planets (Kaspi et al. 2013; Soyuer, Soubiran & Helled 2020). The barotropic nature above this region implies that the observed momentum flux convergence at the cloud level of Jupiter (Salyk et al. 2006) and Saturn (Del Genio et al. 2007) can drive the flow to great depths, perhaps by the downward control principle (Haynes et al. 1991; Liu & Schneider 2010), until dissipation due to rising conductivity and interaction with the magnetic field causes its almost abrupt decay. The downward propagation mechanism was shown to be effective also in the presence of a stable layer (Showman,

Gierasch & Lian 2006), which might also act to decay the flow together with the action of the magnetic field (Christensen, Wicht & Dietrich 2020). Such a stable layer was recently suggested to be necessary for the case of Jupiter (Debras & Chabrier 2019).

The results reported here are also in agreement with simulations of the magnetohydrodynamics of gas giants (Heimpel, Aurnou & Wicht 2005; Gastine & Wicht 2012; Heimpel, Gastine & Wicht 2016; Duarte, Wicht & Gastine 2018), in which strong barotropic flows are found above the fully conducting region, and much weaker baroclinic flows inside it. In the barotropic region, the zonal flow is aligned with the axis of rotation according to the Taylor–Proudman theorem (for the compressible case), and horizontal entropy gradients must be small (Jones 2014). This also implies that the entropy expansion coefficient does not change considerably with depth, as the decay rate of the flow is a product of the entropy gradients and the entropy expansion coefficient (Kaspi et al. 2009). The barotropicity of the neutral region indicates that there is no significant mechanism acting to decay the flow until the semiconducting region is reached. Compared to the gravity-only solution, the restriction of the flow at depth by the magnetic field measurements requires the flow in the neutral region to be larger, in order for the mass advection to be enough to explain the gravity measurements. We expect the results reported in this study, together with the better understanding of the internal structure of Saturn and Jupiter, to enable better explaining the exact mechanism by which the winds on the gas giants are generated, extended into the planet interior, and finally decay at depth.

ACKNOWLEDGEMENTS

DATA AVAILABILITY

The data underlying this article will be shared on request to the corresponding author.

REFERENCES

Atkinson D. H., Pollack J. B., Seiff A., 1996, Science, 272, 842
Bolton S. J. et al., 2017, Science, 356, 821
Cao H., Dougherty M. K., Hunt G. J., Provan G., Cowley S. W. H., Bunce E. J., Kellock S., Stevenson D. J., 2020, Icarus, 344, 113541
Cao H., Stevenson D. J., 2017a, J. Geophys. Res. Planets, 122, 686
Cao H., Stevenson D. J., 2017b, Icarus, 296, 59
Christensen U. R., Wicht J., Dietrich W., 2020, ApJ, 890, 61
Connerney J. E. P. et al., 2018, Geophys. Res. Lett., 45, 2590
Debras F., Chabrier G., 2019, ApJ, 872, 100
Del Genio A. D., Barbara J. M., Ferrier J., Ingersoll A. P., West R. A., Vasavada A. R., Spitale J., Porco C. C., 2007, Icarus, 189, 479
Dougherty M. K. et al., 2018, Science, 362, aat5434
Duarte L. D. V., Wicht J., Gastine T., 2018, Icarus, 299, 206
Duer K., Galanti E., Kaspi Y., 2019, ApJ, 879, L22
Duer K., Galanti E., Kaspi Y., 2020, J. Geophys. Res. Planets, 125, e06292
Fletcher L. N. et al., 2020, J. Geophys. Res. Planets, 125, e06399

French M., Becker A., Lorenzen W., Nettelmann N., Bethkenhagen M., Wicht J., Redmer R., 2012, ApJS, 202, 5
Galanti E., Cao H., Kaspi Y., 2017a, Geophys. Res. Lett., 44, 8173
Galanti E., Kaspi Y., 2016, ApJ, 820, 91
Galanti E., Kaspi Y., 2017, ApJ, 843, L25
Galanti E., Kaspi Y., Miguel Y., Guillot T., Durante D., Racioppa P., Iess L., 2019, Geophys. Res. Lett., 46, 616
Galanti E., Kaspi Y., Tziperman E., 2017b, J. Fluid Mech., 810, 175
Galanti E., Kaspi Y., 2017c, Icarus, 286, 46
García-Melendo E., Pérez-Hoyos S., Sánchez-Lavega A., Hueso R., 2011, Icarus, 215, 62
Gastine T., Wicht J., 2012, Icarus, 219, 428
Gastine T., Wicht J., Duarte L. D. V., Heimpel M., Becker A., 2014, Geophys. Res. Lett., 41, 5410
Haynes P. H., McIntyre M. E., Shepherd T. G., Marks C. J., Shine K. P., 1991, J. Atmos. Sci., 48, 651
Heimpel M., Aurnou J., Wicht J., 2005, Nature, 438, 193
Heimpel M., Gastine T., Wicht J., 2016, Nat. Geosci., 9, 19
Helled R., Galanti E., Kaspi Y., 2015, Nature, 520, 202
Holton J. R., 1992, An Introduction to Dynamic Meteorology, 3rd edn. Acad. Press, Cambridge, MA, USA
Hubbard W. B., 1999, Icarus, 137, 357
Iess L. et al., 2018, Nature, 555, 220
Iess L. et al., 2019, Science, 364, 1052
Jones C. A., 2014, Icarus, 241, 148
Kapyla P. J., Korpi M. J., Ossendrijver M., Stix M., 2006, A&A, 455, 401
Kaspi Y., 2013, Geophys. Res. Lett., 40, 676
Kaspi Y., Flierl G. R., Showman A. P., 2009, Icarus, 202, 525
Kaspi Y., Galanti E., Showman A. P., Stevenson D. J., Guillot T., Iess L., Bolton S. J., 2020, Space Sci. Rev., 216, 84
Kaspi Y., Hubbard W. B., Showman A. P., Flierl G. R., 2010, Geophys. Res. Lett., 37, L01204
Kaspi Y., Showman A. P., Hubbard W. B., Aharonson O., Helled R., 2013, Nature, 497, 344
Kaspi Y. et al., 2018, Nature, 555, 223
Kong D., Zhang K., Schubert G., Anderson J. D., 2018, Proc. Natl. Acad. Sci. USA, 115, 8499
Liu J., Goldreich P. M., Stevenson D. J., 2008, Icarus, 196, 653
Liu J., Schneider T., 2010, J. Atmos. Sci., 67, 3652
Lowes F. J., 1974, Geophys. J. Int., 36, 717
Mankovich C., Marley M. S., Fortney J. J., Movshovitz N., 2019, ApJ, 871, 1
Moore K. et al., 2018, Nature, 561, 76
Moore K. M., Cao H., Bloxham J., Stevenson D. J., Connerney J. E. P., Bolton S. J., 2019, Nat. Astron., 3, 730
Pedlosky J., 1987, Geophysical Fluid Dynamics. Springer-Verlag, New York, p. 710
Porco C. C. et al., 2003, Science, 299, 1541
Qin S., Kong D., Zhang K., Schubert G., Huang Y., 2020, ApJ, 890, 26
Read P. L., Dowling T. E., Schubert G., 2009, Nature, 460, 608
Ridley V. A., Holme R., 2016, J. Geophys. Res. Planets, 121, 309
Salyk C., Ingersoll A. P., Lorre J., Vasavada A., Del Genio A. D., 2006, Icarus, 185, 430
Showman A. P., Gierasch P. J., Lian Y., 2006, Icarus, 182, 513
Smith B. A. et al., 1982, Science, 215, 505
Soyuer D., Soubiran F., Helled R., 2020, MNRAS, 498, 621
Sánchez-Lavega A., Rojas J. F., Sada P. V., 2000, Icarus, 147, 405
Tollefson J. et al., 2017, Icarus, 296, 163
Tsang Y.-K., Jones C. A., 2020, Earth Planet. Sci. Lett., 530, 115879
Wicht J., Gastine T., Duarte L. D. V., 2019a, J. Geophys. Res. Planets, 124, 837
Wicht J., Gastine T., Duarte L. D. V., Dietrich W., 2019b, A&A, 629, A125
Zhang K., Kong D., Schubert G., 2015, ApJ, , 806, 270

APPENDIX A: A MAGNETICALLY RESTRICTED GRAVITY OPTIMIZATION METHOD

The first set of solutions is performed in the following way. First, the magnetic measurements are used to constrain the decay profile in the semiconducting region. Then the TW model is used to find the optimal decay function in the outer non-conducting region, as well as the optimal cloud-level wind, so that the resulting gravity field explains best the gravity measurements. For the Saturn case, the values used as measurements are the *Cassini* measurements (Iess et al. 2019) from which the static body harmonics (Galanti et al. 2019) are subtracted

$$J_n^{\text{dyn}} = J_n^{\text{obs}} - J_n^{\text{rigid}}, \qquad (A1)$$

where J_n^{obs} are the measured gravity harmonics and J_n^{rigid} are the rigid-body solutions taken from the average of an ensemble model solution (Galanti et al. 2019). Note that J_n^{rigid} have non-zero values only for the even harmonics. For the Jupiter case, only the odd gravity measurements are used (Iess et al. 2018), and since these are fully wind induced, there is no need to subtract the solid body contribution (Kaspi et al. 2018).

The parameters to be optimized, i.e. the parameter defining the flow structure above the semiconducting region and the cloud-level wind latitudinal profile, are defined as a control vector

$$\begin{aligned} X_C &= \{X_H, X_u\} \\ &= \left\{ \delta H_T/h_{\text{nor}}, \left[A_1^{\text{sol}}, \cdots, A_N^{\text{sol}} \right] / u_{\text{nor}} \right\}, \end{aligned} \qquad (A2)$$

where $h_{\text{nor}} = 10^7$ and $u_{\text{nor}} = 10^3$ are the normalization factors for the decay structure and the wind coefficients, respectively. The normalization factors are chosen so that $0 < \delta H_T/h_{\text{nor}} < 1$ and $-1 < A^{\text{sol}}/u_{\text{nor}} < 1$. Minimizing the difference between the model solution for the gravity field and the measurements, subjected to the uncertainties of the measurements and the need to keep the optimized control parameters regularized to physical values, is achieved with the cost function

$$L_T = (\boldsymbol{J}^{\text{m}} - \boldsymbol{J}^{\text{o}})\mathbf{W}(\boldsymbol{J}^{\text{m}} - \boldsymbol{J}^{\text{o}})^{\text{T}} + \epsilon_u(\boldsymbol{X}_u - \boldsymbol{X}_o)(\boldsymbol{X}_u - \boldsymbol{X}_o)^{\text{T}}, \quad (A3)$$

where for the Saturn case $\boldsymbol{J}^{\text{m}} = [J_3^{\text{m}}, J_5^{\text{m}}, J_6^{\text{m}}, J_7^{\text{m}}, J_8^{\text{m}}, J_9^{\text{m}}, J_{10}^{\text{m}}]$ and $\boldsymbol{J}^{\text{o}} = [J_3^{\text{dyn}}, J_5^{\text{dyn}}, J_6^{\text{dyn}}, J_7^{\text{dyn}}, J_8^{\text{dyn}}, J_9^{\text{dyn}}, J_{10}^{\text{dyn}}]$ are the calculated and measured gravity harmonics, respectively, $\mathbf{W}$ are the uncertainties in the gravity measurements, $\boldsymbol{X}_o = [A_1^{\text{obs}}, \cdots, A_{99}^{\text{obs}}]/u_{\text{nor}}$ are the observed wind profile parameters, and $\epsilon_u = 5 \times 10^8$ is the weight given to the regularization of the wind solution to the observed one. For the Jupiter case, $\boldsymbol{J}^{\text{m}} = [J_3^{\text{m}}, J_5^{\text{m}}, J_7^{\text{m}}, J_9^{\text{m}}]$ and $\boldsymbol{J}^{\text{o}} = [J_3^{\text{dyn}}, J_5^{\text{dyn}}, J_7^{\text{dyn}}, J_9^{\text{dyn}}]$. The cost function is composed of two terms: The first is the difference between the measured and calculated gravity harmonics, and the second assures that the wind solution does not vary too far from the observed one at cloud level. Given the value of ϵ_U and the large number of coefficients defining the wind latitudinal profile, the regularization of the wind is very strong,

thus ensuring that deviations from the observed cloud-level wind are allowed only if they result in a significantly lower value of the cost function. Given an initial guess for X_C, a minimal value of L is searched for using the Matlab function 'fmincon' and taking advantage of the cost-function gradient that is calculated with the adjoint of the dynamical model (Galanti & Kaspi 2016). Finally, the round mean square error (RMSE) we discuss in Table 1 is calculated by

$$\text{RMSE}_{\text{gravity}} = \frac{1}{7} \sum_N W_{nn} \left(J_n^{\text{m}} - J_n^{\text{o}} \right)^2, \qquad (A4)$$

where $n = 3, 5, 6, 7, 8, 9$, and 10, and $N = 7$, for Saturn, and $n = 3$, 5, 7, and 9, and $N = 4$, for Jupiter.

APPENDIX B: A COMBINED MAGNETIC–GRAVITY OPTIMIZATION METHOD

The solution for the fully optimized Saturn case is obtained in the following way. The overall decay function is fixed to the function obtained in the gravity optimization, and in the optimization process we look for further modifications in the cloud-level wind so that in addition to the residual measured gravity field explained by the thermal model, the residual magnetic field is also explained by the MFED solution. The MFED model solution is compared to the measured field by minimizing, in addition to L_T, the cost function

$$L_M = \epsilon_M \sum_{n=4}^{11} \frac{1}{(e_n)^2} \left(\tilde{g}_n^0 - g_n^0 \right)^2, \qquad (B1)$$

where $\tilde{g}_n^0$ are the MFED model solutions, e_n are the measurements errors (Table 1), and $\epsilon_M = 10^5$ is the weight given the cost function. Note that we take into account only the Gauss coefficients g_4^0 to g_{11}^0 that compose the residual magnetic field. The overall cost function to be optimized is then

$$L = L_T + L_M,$$

and the control vector is now

$$X_C = \{X_u\} = \left\{ \left[A_1^{\text{sol}}, \cdots, A_N^{\text{sol}} \right] / u_{\text{nor}} \right\}, \qquad (B2)$$

so that only the parameters composing the cloud-level wind are optimized. The optimization is done jointly. In each iteration, the temporal solution for the flow structure is used to generate the gravity harmonics with the TW model and the magnetic coefficients with the MFED model. Then, the cost function L is calculated and a modified cloud-level wind is calculated using Matlab 'fmincon'. Finally, the RMSE we discuss in Table 2 is calculated by

$$\text{RMSE}_{\text{magnetic}} = \frac{1}{8} \sum_{n=4}^{11} \frac{1}{(e_n)^2} \left(\tilde{g}_n^0 - g_n^0 \right)^2, \qquad (B3)$$

where $\tilde{g}_n^0$ is the model solution.
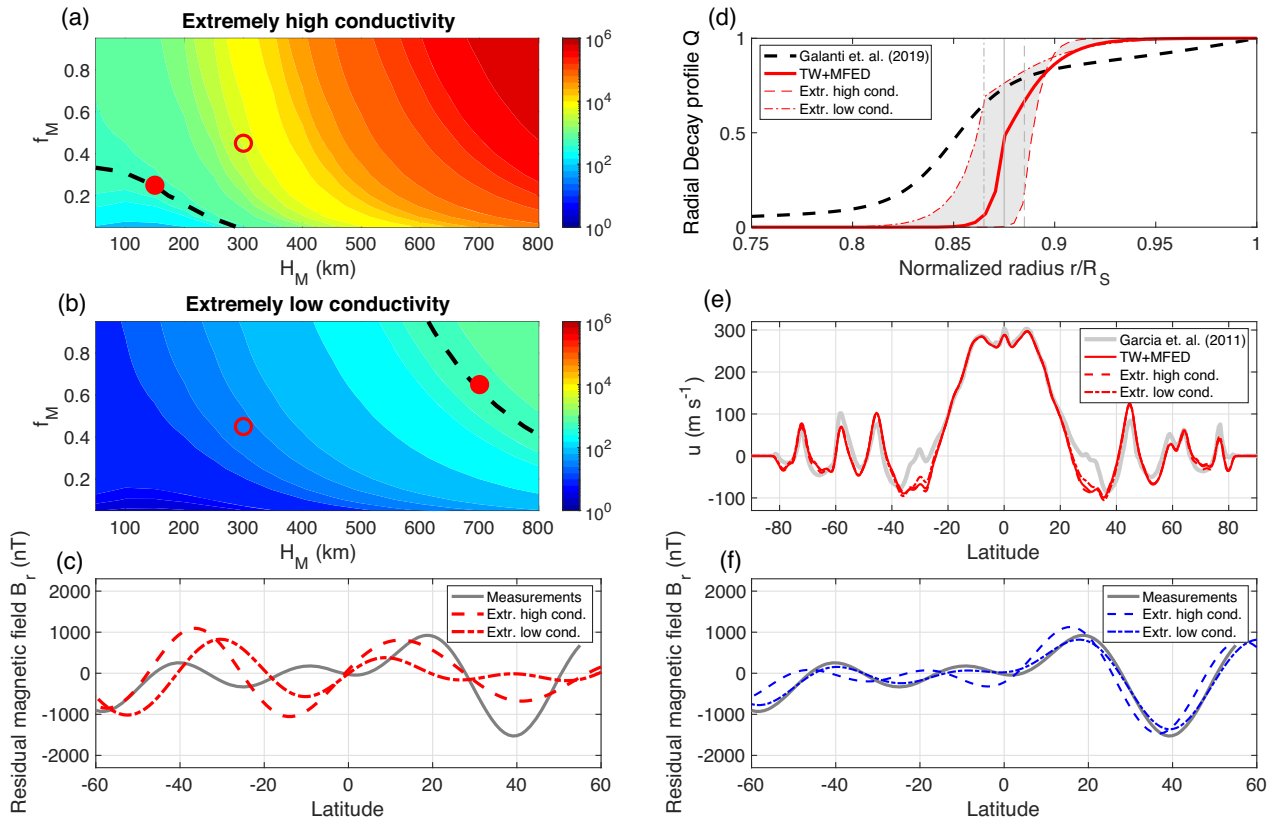
Figure B1. The effect of the uncertainty in the conductivity on the structure of the flow. (a) Similar to Fig. 2(a), but for a case of extremely high conductivity. The parameters ($H_M = 150$, $f_M = 0.25$) result in a wind-induced residual magnetic field fitting the measurements (full red circle), indicating a very low wind in the conductive region. (b) Same as (a) but for a case of extremely low conductivity. The parameters $H_M = 700$ and $f_M = 0.65$ (full red circle), needed for a fit to the measurements, represent a stronger and deep wind in the conductive region. (c) The resulting residual magnetic fields corresponding to the radial flow profiles chosen [full red circles in (a) and (b)]. (d) The solutions for the full radial profiles of the extreme cases (red dashed and dashed–dotted), which allow fitting the gravity field as well. Also shown are the solutions from the main text (solid red), and the gravity-only (Galanti et al. 2019 solution; black). Note that the transition depth R_T is different for each case, denoting the depth where $\sigma = 10^{-2}\,\mathrm{S\,m^{-1}}$. (e) The cloud-level wind solutions for the two extreme cases. (f) The optimal solution of the residual magnetic field for the two extreme cases (blue dashed and dashed–dotted).

APPENDIX C: UNCERTAINTIES IN THE MFED MODEL

The electrical conductivity σ (see Section 2), essential to the determination of the wind-induced magnetic field, is known within two orders of magnitude in both Jupiter and Saturn (Liu et al. 2008; Wicht et al. 2019b), and therefore the effect of its uncertainty on the radial profile (Fig. 3) should be evaluated. While the uncertainty in the electrical conductivity is indeed very large, its effect on the wind-induced magnetic field is less dramatic, due to the exponential nature of its dependence on depth. To illustrate this, we examine two extreme scenarios discussed in the literature (Liu et al. 2008): one in which the conductivity is an order of magnitude larger and one in which it is an order of magnitude lower than the mean value. The results are presented in Fig. B1. In both cases, a radial profile of the flow in the semiconducting region can be found (Figs B1a, b) such that the magnitude of the induced residual magnetic field is similar to the measured one (Fig. B1c). Next, in both cases, a radial profile in the outer region can be found such that the gravity measurements are also explained (Fig. B1d), with a modified cloud-level wind that is very similar to the solution with regular conductivity (Fig. B1e). The RMSEs for the high and low extreme cases are 0.70 and 0.34, respectively. Note that in the case with the extreme low

conductivity, the gravity is slightly easier to match than the standard case. Finally, a fully optimized solution that can explain both the gravity and magnetic measurements can be found for both extreme cases. The gravity RMSEs are now 0.92 and 0.30 for the high and low cases, respectively. The magnetic RMSEs are now 1.90 and 0.47. Note that, similar to the solutions without fitting the magnetic field details, it is easier to fit the magnetic field latitudinal structure with the extreme low conductivity and somewhat more difficult with the extremely high values. The solutions for both extreme cases show a similar behaviour in the outer region where the flow is found to be mostly barotropic. They also show a similar behaviour in having no tail in deep layers. The shift in the depth of the winds between the two extreme cases (grey region in Fig. B1d) is about 1000 km, and both solutions are distinctively different from the gravity-only (Galanti et al. 2019) solution (dashed black). With that, it is evident that the stronger electrical conductivity results in a sharper decay of the winds, and the weaker conductivity results in a more moderate decay that is closer to the shape obtained when fitting only the gravity field.

Based on the above analysis, we can also discuss even more extremes values of the conductivity. The solution with the order of magnitude higher conductivity is already not as good as the regular one (Fig. B1f), and more importantly, further increase in the value

will push the shape of the decay function in the semiconducting region to be unphysical. This is evident in Fig. B1(a), where the values defining the decay function, H_M and f_M, are already quite close to zero for the extreme case (solid red dot). Solving the model with another order of magnitude larger conductivity makes the problem unsolvable. In addition, the high conductivity already pushes the winds to be completely barotropic in the outer region (Fig. B1d, dashed red line). As we discuss in Section 3.1.1, this is necessary in order to explain the gravity harmonics, since this extreme decay function involves less mass (weaker winds) in the semiconducting zone, and therefore more mass (stronger winds) has to be included in the outer region. Pushing the decay depth even closer to the surface will not allow a fit to the gravity measurements. As for the extremely weak conductivity, there our model does not pose any constraint. The weaker the conductivity (or α-effect) is, the more the solution becomes similar to the gravity-only solution, and there can always be a larger value for H_M to define the exponential decay in the semiconducting region.

Another source for uncertainty is the dynamo α-effect of which the latitudinal dependence is not well known (Cao & Stevenson 2017b). However, modifying the latitudinal dependence of the α-effect, as well as adding the γ-effect (Kapyla et al. 2006), might add complexity to the solution but would not change the main results (Cao & Stevenson 2017b; Galanti et al. 2017a). First, the magnitude of α would not be significantly different. Secondly, while the latitude dependence of the solution will change, but as demonstrated here, with minor modification of the cloud-level wind, the details of the measurements can be explained by the model solution. Finally, under the assumptions taken in the MFED of small-scale turbulence in the entire semiconducting region, modifying the overall magnitude of the dynamo α-effect is equivalent in general to changing the value of the conductivity (see equation 4); therefore, the exploration above should suffice to account for that uncertainty. With that, it should be noted that a strongly stratified layer would disconnect the region below it from the winds above, and render the α-effect to be smaller. However, such a stable layer, if existed, is expected to be in deeper layers (Debras & Chabrier 2019).

APPENDIX D: ESTIMATES FOR THE MAGNETIC REYNOLDS NUMBER

A basic requirement for using the MFED balance is that the magnetic Reynolds number would satisfy $R_m(u) < 1$ [Cao & Stevenson 2017b; it is defined as $R_m(u) = uH_\sigma\sigma\mu_0$, where $u(r, \theta)$ is the flow velocity, σ is the electrical conductivity, and $H_\sigma = \sigma/\frac{d\sigma}{dr}$ is the scale height associated with it]. In Fig. D1(a), we show $R_m(u)$ calculated with the Saturn's optimal flow solution (Fig. 3a), where the maximal value in the semiconducting region is 0.98; thus, the condition is satisfied. Note that $R_m(u)$ becomes extremely small close to the lower boundary because the modelled flow goes to zero there, while in reality the flow
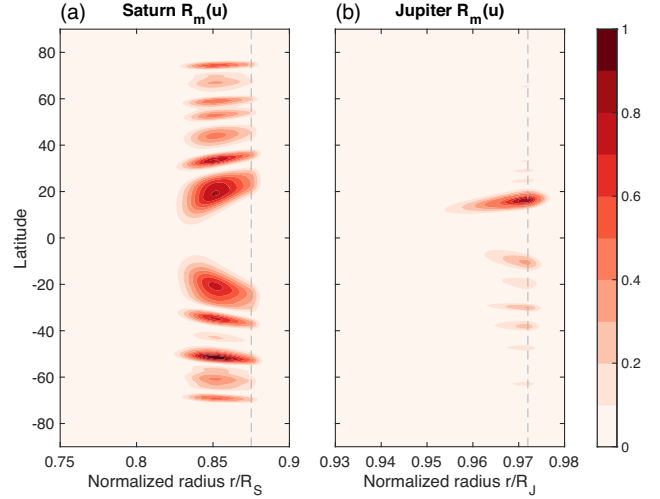
Figure D1. The magnetic Reynolds number $R_m(u)$ for the Saturn (a) and Jupiter (b) solutions, in the semiconducting region. In the Saturn case $R_m(u)^{\max} = 0.98$ and in the Jupiter case $R_m(u)^{\max} = 0.88$. Thus, in both cases the basic requirement that enables using the MFED balance, $R_m(u) < 1$, is met.

strengthens, and so $R_m(u)$ might be higher there. This has practically no effect on our results and conclusion since the gravity harmonics are not sensitive to $O(1)$ m s^{-1} variations at these depths. Moreover, the wind-induced residual magnetic field B_r can be roughly related to the background field $\boldsymbol{B_0}$ via $B_r \sim R_m(\alpha)^{\max}R_m(u)^{\max}|\boldsymbol{B_0}|$, where $R_m(\alpha) = \alpha H_\sigma\sigma\mu_0$ is the magnetic Reynolds number associated with the dynamo α-effect (Cao & Stevenson 2017b). Since $R_m(\alpha)$ reaches a maximal value of 0.25 (at the lower boundary of the semiconducting region) and $R_m(u) < 1$ everywhere, the resulting residual magnetic field is ensured to be much smaller than the background field (Fig. 2b). With that, the $R_m(u)$ associated with our solution is close to 1 in some regions indicates that the actual flow in the semiconducting region, especially in its outer part, might be weaker than our solution. The measured residual magnetic field will then not be solely due to the winds (see above discussion). In such a case, the decay of the wind around the 7000 km depth would be even sharper. A similar analysis was performed with Jupiter's optimal solution (Fig. 4a). The magnetic Reynolds number associated with this solution (Fig. D1b) has a maximum value of 0.88 in that region, and is less than 0.1 in most of the domain, thus ensuring that the wind-induced residual magnetic field will be much smaller than the internal field. Note that other methods for estimating $R_m(u)$ might be used (Wicht, Gastine & Duarte 2019a), but this should not affect substantially the results shown here.

This paper has been typeset from a TEX/LATEX file prepared by the author.